PAPER

Check for updates

View Article Online
View Journal

Cl-Loss dynamics in the dissociative photoionization of CF_3Cl with threshold photoelectron–photoion coincidence imaging†

Xiangkun Wu,[a] Guoqiang Tang,[a] Hanhui Zhang,[a] Xiaoguo Zhou, (ID) *[a] Shilin Liu, (ID) [a] Fuyi Liu,[b] Liusi Sheng[b] and Bing Yan[c]

The dissociative photoionization of CF_3Cl was investigated in the photon energy range of 12.30–18.50 eV. The low-lying electronic states of CF_3Cl^+ cations were prepared by the method of threshold photoelectron–photoion coincidence (TPEPICO). The threshold photoelectron spectrum and the coincident time-of-flight mass spectra at the specific photon energies were recorded. Only a CF_3^+ fragment was observed at lower energy, while a CF_2Cl^+ fragment appeared for C^2E and D^2E states. As Cl-loss from the ground ionic state is statistical, the total kinetic energy release distribution (KERD) is represented as a Boltzmann profile, and a 0 K appearance energy of $AP_0 = 12.79 \pm 0.02$ eV is derived from the statistical modelling of the breakdown diagram from 12.60 to 12.85 eV without taking into account the kinetic shift. For the A^2A_1 and B^2A_2 states of CF_3Cl^+ cations, the total KERDs are bimodal, where a parallel faster dissociation appears together with the statistical distribution. At higher energies like the C^2E and D^2E ionic states, a bimodal distribution similar to that of the A^2A_1 and B^2A_2 states is also observed for the KERD. With the aid of the calculated Cl-loss potential energy curves, the dissociative mechanisms of internal energy-selected CF_3Cl^+ cations are proposed.

1. Introduction

Halogenated methane has been extensively applied in practical industry, *e.g.* the plasma etching of silicon wafer semi-conductor devices,[1,2] highly reactive plasma reactions, and so on.[3] However, halogenated methane is believed to play a major role in the depletion of ozone in the stratosphere,[4] because it can be dissociated by solar UV light to produce halogen atoms. As a typical chlorofluorocarbon, CF_3Cl can produce chlorine atoms with UV photolysis as well, and thus its dissociation and dissociative photoionization are worthy of attention.

The ground state of neutral CF_3Cl molecules has C_{3v} geometry, and the valence-shell electron configuration is $...(3a_1)^2(2e)^4(4a_1)^2$-$(3e)^4(4e)^4(1a_2)^2(5a_1)^2(5e)^4$, where the non-bonding orbital of $(5e)$ consists of the lone pair of chlorine atoms, the $(5a_1)$ orbital is associated with the $\sigma(C–Cl)$ bond, and the $(1a_2)$, $(4e)$ and $(3e)$ electrons are essentially supplied by the lone pair of fluorine atoms.[5–7] By removing an electron from the outer orbitals, *e.g.* $(5e)$, $(5a_1)$, $(1a_2)$, $(4e)$ or $(3e)$, CF_3Cl^+ ions in the X^2E, A^2A_1, B^2A_2, C^2E and D^2E states can be produced. Using He I and He II photoionization, the photoelectron spectra (PES) of CF_3Cl was obtained,[5–7] where the low-lying electronic states were assigned. Different from the structureless spectra of A^2A_1, B^2A_2 and C^2E, a series of vibrational bands were observed for the D^2E state, and the assignments were obtained. Similar conclusions were reported in the PES[8] and threshold photoelectron spectra (TPES)[9,10] using the VUV light of synchrotron radiation. Vertical ionization potentials for X^2E were measured to be 13.00 eV, 13.08 eV, and 13.1 eV in different experiments.[6,7,11–13] The adiabatic ionization potential of CF_3Cl was determined to be 12.39 eV,[14,15] 12.45 eV,[9] 12.60 eV[16] and 12.91 eV[17] with the method of photoionization, 13.0 eV in electron impact ionization[18] and 12.50 eV in dipole coincidence spectroscopy.[19] The appearance energy (AP) was obtained as well, and $AP(CF_3^+/CF_3Cl) = 12.55$ eV,[9] 12.63 eV,[14] 12.65 eV[15] and 12.75 eV.[10] The APs of the other fragments were determined as $AP(CF_2Cl^+/CF_3Cl) = 14.25$ eV,[9,20] 14.3 eV,[10] 14.5 eV[19] and 15.0 eV[18] and $AP(CF_2^+/CF_3Cl) = 18.85$ eV.[9,21] By applying the DFT-B3LYP and G3X level of theory, the adiabatic ionization energies and the appearance energies were calculated and compared with the experimental data.[22,23] Furthermore, the photoionization cross sections of various valence shells of CF_3Cl were estimated.[24–26]

[a] Hefei National Laboratory for Physical Sciences at the Microscale, iChEM (Collaborative Innovation Center of Chemistry for Energy Materials), Department of Chemical Physics, University of Science and Technology of China, Hefei, Anhui 230026, China. E-mail: xzhou@ustc.edu.cn

[b] National Synchrotron Radiation Laboratory, University of Science and Technology of China, Hefei, Anhui 230029, China

[c] Institute of Atomic and Molecular Physics, Jilin University, Changchun 130012, China

† Electronic supplementary information (ESI) available. See DOI: 10.1039/c7cp07502b

Only a few experiments have been performed to investigate the dissociation of state-selected CF_3Cl^+. Through analyzing the flight time profiles of mass spectra, Powis and Danby[27] obtained the kinetic energy release distribution (KERD) of CF_3^+ fragments dissociated from X^2E, which was consistent with the Langevin model. For the A^2A_1 and B^2A_2 states, a bimodal distribution was observed in the Cl-loss process including one statistical and one non-statistical dissociation channel. Only the CF_2Cl^+ fragment ion was detected in the dissociation of CF_3Cl^+ at C^2E and D^2E states.[20] However, when using VUV synchrotron radiation as a light source, Creasey et al.[10] observed that the CF_3^+ fragment dissociated from C^2E and D^2E states. Through fitting the TOF profiles, they obtained the KERD and drew the conclusions that the Cl-loss from the A^2A_1/B^2A_2 states is non-statistical, while the C^2E and D^2E states can statistically dissociate along the C–Cl bond rupture.

Recently, we have investigated the dissociative photoionization of a few methyl halides, e.g. CH_3Cl,[28] CH_3Br[29] and CF_4.[30] With the increase of halogen atoms, the ground state of molecular ions becomes less stable, and CF_4 does not even form a stable parent ion, but dissociates by F-loss to yield CF_3^+ upon photoionization. In order to reveal the stability of the ground ionic state and the dissociation mechanism of CF_3Cl^+ in low-lying electronic states, threshold photoelectron photoion coincidence (TPEPICO) velocity map imaging has been applied. As an upgraded experimental approach, it is powerful to analyze the dissociation of internal energy-selected cations.[31–33] Compared with the method of fitting TOF profiles to obtain the KERD, the TPEPICO velocity map imaging can provide a more exact KERD and the angular distribution of fragments simultaneously.[34–38] Here, the dissociative photoionization of CF_3Cl in a photon energy range of 12.30–18.50 eV has been carefully reinvestigated. At the specific photon energy, the KERD and angular distribution of CF_3^+ fragments are measured. With the aid of the Cl-loss potential energy curves of CF_3Cl^+ in low-lying states, the dissociation mechanisms of X^2E, A^2A_1, B^2A_2, C^2E and D^2E are proposed.

2. Experimental and computation

All the experiments were performed on the U14-A beamline of the National Synchrotron Radiation Laboratory, Hefei, China. The configurations of the beamline and the TPEPICO velocity map imaging spectrometer were described previously,[32] and only a brief description is introduced here. The VUV photons of synchrotron radiation were produced from an undulater and dispersed with a monochromator. The photon energy range was 7.5–22.5 eV with a resolving power, $E/\Delta E$, of ~ 2000. The higher-order harmonic radiation of the beamline was absorbed by more than 99% by a gas filter filled with neon gas. The absolute energy of the VUV photons was calibrated in TPES using the well-known ionization energies of argon and neon, and the photon flux was measured with a silicon photodiode.

The 99.9% CF_3Cl gas was injected into the vacuum chambers through a 30 μm-diameter nozzle. The typical stagnation pressure was 1.0 atm. The background pressures in the source and

ionization chambers were 2×10^{-3} Pa and 2×10^{-5} Pa, respectively, with the molecular beam on. After being collimated by a 0.5 mm-diameter skimmer, the molecule beam was intersected with the VUV light at 10 cm downstream from the nozzle. Once photoionization had occurred, photoelectrons and photoions were driven along opposite directions by a direct current extraction field (~ 15 V cm^{-1}). Double velocity map imaging was applied to collect both threshold electrons and ions simultaneously. As indicated in previous investigations,[32] the contamination of hot electrons (with a certain kinetic energy) was efficiently suppressed using the decelerated electric field[39] and the subtraction method.[40] The TPEPICO TOF mass spectra were obtained with a single-start multiple-stop data acquisition mode,[41] in which the threshold photoelectrons were used as the start signals for the flying time of ions. Velocity map images of the ions were directly projected on two 40 mm-diameter multichannel plates backed by a phosphor screen (Burle Industries, P20), and were recorded by a thermoelectric-cooling charge coupled device camera (Andor, DU934N-BV). A pulsed high voltage (DEI, PVM-4210) was applied at the MCPs of ions as a mass gate to record the time-sliced velocity map image of the coincident ion. The minimum effective duration time of the mass gate was ~ 40 ns in the present experiment.

All theoretical calculations were performed with the Gaussian 09W program package (D.01 version 9.5).[42] The geometries of neutral CF_3Cl and its ground-state cations were optimized with density functional theory (DFT) with B3LYP/6-311+G(d) basis sets. The optimized geometries of the electronic excited states of CF_3Cl^+ were calculated using the TD-DFT/6-311+G(d) level of theory. A partial optimization method was applied to obtain the Cl-loss potential energy curves of the electronic states, in which the lowest eight electronic states were involved. At every given C–Cl distance, the other geometry parameters were re-optimized. The electronic configuration of the ionic state was carefully checked to confirm symmetries in the open-shell excited species. The ionization energies of the ionic states were calculated at the EOM-CCSD/cc-PVTZ level,[43–46] with the optimized geometries.

3. Result and discussion

A. Optimized geometries of CF_3Cl^+ in low-lying electronic states

Table 1 summarizes the optimized geometries and the vertical ionization energies of CF_3Cl^+ in the low-lying electronic states. With the loss of a Cl atom, the symmetry of CF_3Cl^+ is degenerated from C_{3V} to C_S. Thus the original ^2E state in C_{3V} symmetry is divided into the $^2A'$ and $^2A''$ in C_S symmetry, and the $^2A_1$ and $^2A_2$ states correspond to $^2A'$ and $^2A''$ states. The two components $^2A'$ and $^2A''$ of the X^2E state are nearly degenerate, and their ionization potentials are calculated to be 12.52 eV after correction of zero-point energy. The optimized C–Cl bond length is 2.388 Å and much larger than that of the neutral ground state, R(C–Cl) = 1.773 Å, thus, its potential well is far from the Franck–Condon region.

As shown in Table 1, the B^2A'', $C(^2A'/^2A'')$ and $D(^2A'/^2A'')$ states are bound, while the $2^2A'$ (A^2A_1) state is repulsive without

Table 1 Optimized geometries and vertical ionization energies (IEs) of CF_3Cl^+ cations in low-lying electronic states

	Symmetry	R(C–Cl)/Å	R(C–F_1)/Å	R(C–F_2)/Å	A(F_1CCl)/°	A(F_2CCl)/°	D(F_2CCl$F_2{'}$)/°	IE[a]/eV Cal.	Exp.
CF_3Cl^+									
X	$^2A'/^2A''(^2E)$	2.388	1.257	1.259	99.28	97.87	119.80	12.52	13.0,[b] 13.15,[c] 13.08[d]
B	$^2A''(^2A_2)$	1.767	1.390	1.311	112.66	112.09	126.38	14.76	15.0,[b,c] 15.20[d]
A	$^2A'(^2A_1)$	—	—	—	—	—	—	16.07	15.5,[b,c] 15.8[d]
C	$^2A''(^2E)$	1.807	1.393	1.311	110.21	111.81	127.26	16.70	16.5,[b] 16.6,[c] 16.72[d]
	$^2A'(^2E)$	1.805	1.320	1.362	112.74	113.53	116.13	16.72	
D	$^2A''(^2E)$	1.758	1.368	1.373	114.48	110.30	125.09	17.73	17.4,[b] 17.5,[c] 17.71[d]
	$^2A'(^2E)$	1.776	1.376	1.366	107.43	113.48	117.57	17.73	
CF_3Cl									
X	$^1A'(^1A_1)$	1.773	1.333	1.333	110.32	110.35	120.00	0.0	

[a] IEs were corrected with a zero-point energy of 0.38 eV, which was obtained by a scaled factor of 0.95 and the harmonic frequencies at B3LYP/6-311+G*. [b] From ref. 7. [c] From ref. 9. [d] From ref. 5.

a well on its potential energy surface. This is reasonable because an electron of the σ(C–Cl) bond is removed during photoionization for the A^2A_1 state. The vertical ionization energies are calculated as 14.76 eV for B^2A'', 16.07 eV for A^2A', 16.70 eV for C^2A'', 16.72 for C^2A' and 17.73 eV for D($^2A'/^2A''$), and are generally consistent with the experimental data.[5,7,9] Moreover, the optimized C–Cl bond lengths in the B^2A'', C($^2A'/^2A''$) and D($^2A'/^2A''$) states are in a range of 1.76–1.81 Å and close to that of the neutral ground state.

B. Cl-Loss potential energy curves of CF_3Cl^+

Although the TD-DFT method is based on a single reference configuration, the potential energy curves of the electronic excited states of halogenated hydrocarbons can be qualitatively described like $C_2H_3F^{+}$[47] and $C_2H_3Cl^{+}$.[48] Thus, the TD-DFT/B3LYP method was applied to calculate the Cl-loss potential energy curves of CF_3Cl^+ in low-lying electronic states.

Fig. 1 shows the calculated adiabatic potential energy curves of low-lying electronic states along the C–Cl distance. The X($^2A'/^2A''$) and A^2A' states are adiabatically correlated to the lowest dissociation channel of $CF_3^+(^1A_1)$ + Cl(^2P), while the B^2A'', C($^2A'/^2A''$) and D($^2A'/^2A''$) states adiabatically correlate to the excited $CF_3^+(A^1E)$ + Cl (^2P) channel. As indicated by the potential energy surfaces with the frozen structure assumption (in Fig. S1 of the ESI†), coupling from the higher electronic states can be neglected due to the too high excitation energy. Therefore, the dissociation of B^2A'', C($^2A'/^2A''$) and D($^2A'/^2A''$) can only process via internal conversion to the lower electronic states according to the too high energy of the $CF_3^+(A^1E)$ + Cl(^2P) dissociation limit. On the contrary, the dissociation of A^2A' is a typically rapid process along a repulsive potential energy curve. In addition, the energy of the X($^2A'/^2A''$) state is very close to the dissociation limit in the Franck–Condon region, and thus it can statistically dissociate with the increase of the internal energy of cations.

Moreover, there is a curve-crossing between the A^2A' and B^2A'' states near the photoionization region, which will cause an overlap between them in the threshold photoelectron spectrum (TPES). The contribution of the repulsive A^2A' state should be dominant in the higher energy of the overlapping band in the TPES because its vertical excitation energy is higher than that of the bound B^2A'' state.
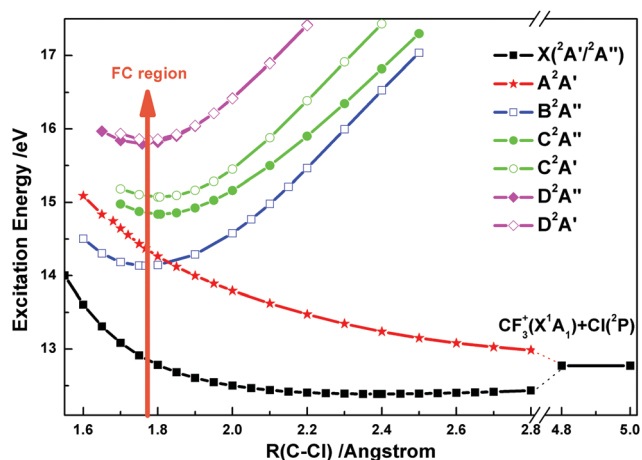

Fig. 1 Cl-Loss potential energy curves of the low-lying electronic states of CF_3Cl^+ at the TD-B3LYP/6-311+G(d) level, where the orange arrow indicates photoionization from the neutral molecule in the Franck–Condon region.

C. Threshold photoelectron spectrum of CF_3Cl

Fig. 2 shows the threshold photoelectron spectrum of CF_3Cl in the excitation energy range of 12.30–18.50 eV, where the step size was 10 meV. Several structureless peaks were contributed by the five low-lying electronic states of CF_3Cl^+, X^2E, A^2A_1, B^2A_2, C^2E and D^2E. Although no vibrational structure can be resolved, the ionization energy (IE) can be estimated to be 12.46 eV from the beginning energy of X^2E, which agrees with the previous data derived from photoionization effective curves and theoretical calculations.[9,14,15,22,23] It is a bit undervalued because the Franck–Condon region is quite far from the ionic minimum. As suggested by previous studies,[5,9] the second band with weak intensity consists of both the A^2A_1 and B^2A_2 states, which are very close in energy. The following two bands are attributed to the C^2E and D^2E states, respectively. The resonance energies and relative intensities of these bands are consistent with the previous TPES.[10] The energies of these peaks also generally agree with the vertical IEs calculated at the EOM-CCSD/cc-PVTZ level in Table 1. Cvitas et al.[5] observed a few weak vibrational bands of D^2E in the photoelectron spectrum with a poor signal to noise ratio but the structure did not exist in Fig. 2, implying that the
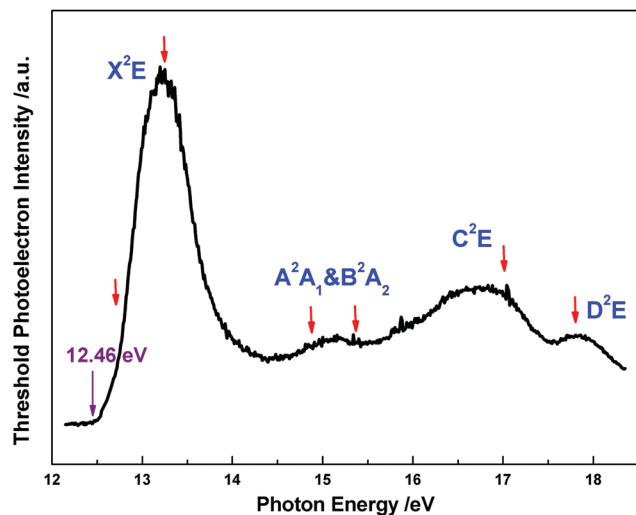
Fig. 2 Threshold photoelectron spectrum of CF_3Cl in the excitation range of 12.30–18.50 eV, where the coincident mass spectra were recorded at the specific photon energies noted by the arrows.

vibrational structures were probably contaminated by the auto-ionization of high Rydberg states. Six specific photon energies noted by the arrows in Fig. 2 have been selected for the following investigation of dissociative photoionization, *i.e.* 12.75, 13.26, 14.88, 15.36, 16.99 and 17.85 eV.

D. TPEPICO time-of-flight mass spectra

The TPEPICO mass spectra were obtained with an extraction electric field of 15 V cm^{-1} and are shown in Fig. 3. At the lower energy, both $CF_3{}^{35}Cl^+$ and $CF_3{}^{37}Cl^+$ parent ions were located at 21.08 and 21.28 μs, with full widths at half maximum (FWHM) of 38 ns. With an increase in photon energy, the $CF_3{}^+$ fragment ion appeared at 16.99 μs and the parent ions gradually disappeared. The TOF profile of $CF_3{}^+$ was observed as a slightly asymmetric contour only at the onset and became symmetric with the increase in photon energy, indicating a metastable dissociation with nonsignificant kinetic shift. Moreover, a broadened
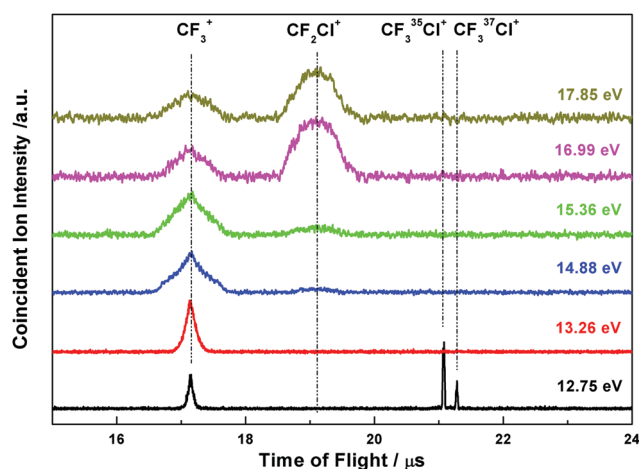
triangular shape of the $CF_3{}^+$ TOF profile implies that the kinetic energy release happens in the C–Cl bond rupture.

Interestingly, the TOF profile of $CF_3{}^+$ fragments dissociated from the A^2A_1 and B^2A_2 states (blue and green curves in Fig. 3) looks like a broadened triangle superimposed over a near rectangular background, indicating that at least two Cl-loss pathways exist for CF_3Cl^+ in A^2A_1 and B^2A_2 states. Moreover, more fragment ions were observed with the increase in photon energy. The CF_2Cl^+ fragment ion appeared with a very limited fraction at 14.88 and 15.36 eV (A^2A_1 and B^2A_2), and gradually became the dominant fragment at the high excitation energy C^2E and D^2E states. In addition, the full widths of the $CF_3{}^+$ and CF_2Cl^+ peaks in Fig. 3 are expanded to more than 1 μs for all the electronic excited states, indicating that a lot of energy is released to translation in dissociation.

To our surprise, the width of the $CF_3{}^+$ fragment along the same lowest dissociation channel, $CF_3Cl^+ \rightarrow CF_3{}^+ + Cl$, does not markedly change, although the excess energy is increased a lot from the A^2A_1 to D^2E states. A similar phenomenon also exists for CF_2Cl^+ in the C–F bond rupture. Therefore, a complicated dissociation mechanism is expected for the electronic excited states of CF_3Cl^+, where the partially available energy is probably kept as internal energy of fragments in dissociation. More detailed information regarding energy population is necessary for conclusion, and thus the velocity map images of $CF_3{}^+$ and CF_2Cl^+ fragments have been recorded.

E. C–Cl bond dissociation energies of CF_3Cl^+ and the ionization energy of CF_3

The fractional ion abundance of the parent and fragment ions is plotted as a function of photon energy in the breakdown diagram of Fig. 4. As the CF_3Cl^+ signal vanishes, the $CF_3{}^+$ signal rises synchronously due to the C–Cl bond rupture. A statistical model has been constructed for the Cl-loss pathway with the aid of the computed vibrational frequencies and rotational
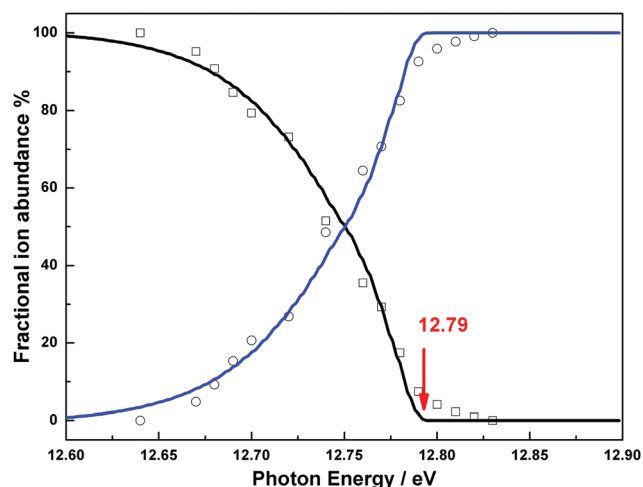

Fig. 3 TPEPICO time of flight mass spectra at the photon energies of 12.75, 13.26, 14.88, 15.36, 16.99 and 17.85 eV.

Fig. 4 Breakdown diagram of CF_3Cl between 12.60 and 12.85 eV, where the shapes correspond to the measured fractional abundances and the lines are the best-fitted data, based on which the appearance energy at 0 K is determined.

constants. The statistical modelling has been described in detail by Sztáray *et al.*,[49] and successfully applied to obtain AP_0 in similar halogenated alkanes.[50–52]

In threshold photoionization, the internal energy of CF_3Cl^+ was the sum of the internal energy of the neutral ground state and the photon energy minus the adiabatic ionization energy. The density of states of the parent ion and the number of states of the transition state were used to calculate the unimolecular dissociation rate constant according to the RRKM theory.[53–55] As the symmetric TOF profiles of CF_3^+ were observed just above the onset, a nonsignificant kinetic shift was expected, thus, the 0 K appearance energy was fitted to reproduce the fractional ion abundances without taking into account the kinetic shift here. As indicated by the best fitted curve in Fig. 4, the $AE_0(CF_3^+/CF_3Cl)$ is 12.79 ± 0.02 eV and agrees with the previous data.[8,10,11,19]

At the B3LYP/6-311+G(d) or CBS-APNO level, the deviation of the adiabatic ionization energy of $IE(CF_3Cl)$ between 0 K and 298.15 K is less than 0.04 eV. Thus, $IE_0(CF_3Cl)$ is estimated as *ca.* 12.50 eV. Taking the aforementioned $AE_0(CF_3^+/CF_3Cl)$, the C–Cl bond dissociation energy (BDE) of CF_3Cl^+ is equal to 27.98 ± 3.86 kJ mol^{-1} according to eqn (R1). Using the BDE of a C–Cl bond in a neutral molecule, 3.73 ± 0.01 eV in the 1.122 version of the Active Thermochemical Tables (ATcT),[56–61] the adiabatic ionization energy (IE_0) of the CF_3 radical is calculated to be 9.06 ± 0.02 eV, which is closer to the previous experimental and calculated value ~ 9.0 eV,[50,51,62–72] instead of < 8.8 eV which was derived from the dissociation of CF_3Br^+ and $C_3F_8^+$.[73–75] Interestingly, the $IE_0(CF_3)$ in the 1.122 version of the ATcT is reported to be 9.06 eV from chemical thermodynamics calculations, and is in excellent agreement with our data, indicating that the estimated $IE_0(CF_3Cl)$ and $AE_0(CF_3^+/CF_3Cl)$ should be reliable.

$$BDE(\text{C–Cl in } CF_3Cl^+) = AE_0(CF_3^+/CF_3Cl) - IE_0(CF_3Cl) \quad (R1)$$

$$BDE(\text{C–Cl in } CF_3Cl) = AE_0(CF_3^+/CF_3Cl) - IE_0(CF_3) \quad (R2)$$

As mentioned above, the ionization energy of CF_3Cl is close to the lowest dissociation limit of cations, and thus the kinetic energy distribution of CF_3^+ is represented statistically at 13.26 eV of X^2E as a Boltzmann curve in Fig. 5. As shown in Fig. 1, there is a very shallow well on the Cl-loss potential energy curve of X^2E but it is far from the Franck–Condon region. Therefore, the dissociating time is typically longer than an overall molecular rotational period, and the angular distribution of the fragment is isotropic as we observed in the CF_3^+ image. The conclusion agrees with the result of the statistical dynamical calculations combined with the Langevin model for ion-induced dipole potential.[27]

F. TPEPICO velocity map images of CF_3^+ dissociated from A^2A_1 and B^2A_2 states

As the A^2A_1 and B^2A_2 states are overlapping in the TPES, two specific photon energies, 14.88 eV and 15.36 eV, are chosen in the range to compare the ion images of CF_3^+. Fig. 6 shows the 3-dimensional time-sliced images, where the molecular beam and the electric vector ε of a VUV photon are vertical. At the two
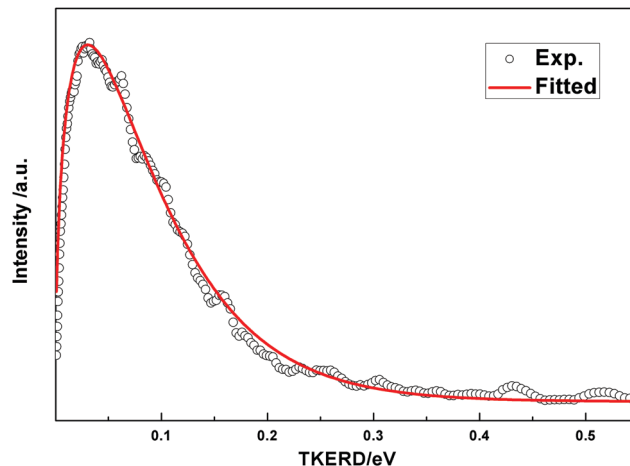

Fig. 5 Total kinetic energy release distribution of CF_3^+ at 13.26 eV.

energies, similar images are observed and include one outer ring and a bright inner spot, indicative of at least two dissociation pathways. By accumulating the intensity of the image over the angle, the speed distribution of CF_3^+ is acquired. Based on the conservations of linear momentum and energy, the total kinetic energy release distribution (KERD) is finally obtained and shown in Fig. 6 as well.

As shown in Fig. 6, the total KERD curves can be fitted very well with Boltzmann- and Gaussian-type curves. Based on the calculated potential energy curves in Fig. 1, the statistical channels of Boltzmann distribution must be contributed by the internal conversion from the bound B^2A'' state to the high vibrationally excited ground state of CF_3Cl^+, followed by a statistical dissociation. The Gaussian profile distribution occupies a large proportion of the total KERD, indicating that the non-statistical dissociation pathway dominates in this energy region. It is naturally contributed to by direct dissociation of the repulsive A^2A' state. As indicated in Table 2, the branching ratio ρ of the rapid dissociation is increased greatly with an increase in photon energy, which roughly corresponds to the proportions of the A^2A' and B^2A'' states in the specific energies. Thus, the contribution of the A^2A' state becomes more significant at a higher energy, which is consistent with the aforementioned theoretical prediction.

For the dissociation along a repulsive potential energy curve, the classical "impulsive model" can be used to estimate the proportion of average total kinetic energy $\langle E_T \rangle$ and available energy E_{avail} with the following formula (1),

$$f_T = \frac{\langle E_T \rangle}{E_{avail}} = \frac{\mu_{C-Cl}}{\mu_{CF_3-Cl}} = 0.383 \quad (1)$$

where μ is the reduced mass. At 14.88 eV and 15.36 eV, both the f_T values are close to the predicted value (0.383). Thus, the rapid dissociation should occur along the repulsive curve of the A^2A' state. As suggested by the "impulsive model", the C_{3V} geometry of the CF_3 group is initially kept while the Cl atom and CF_3 recoil sharply and separate, and the umbrella vibration of CF_3^+ is distributed from the initial recoiled kinetic energy. Taking into account the dissociation limit and the umbrella vibrational
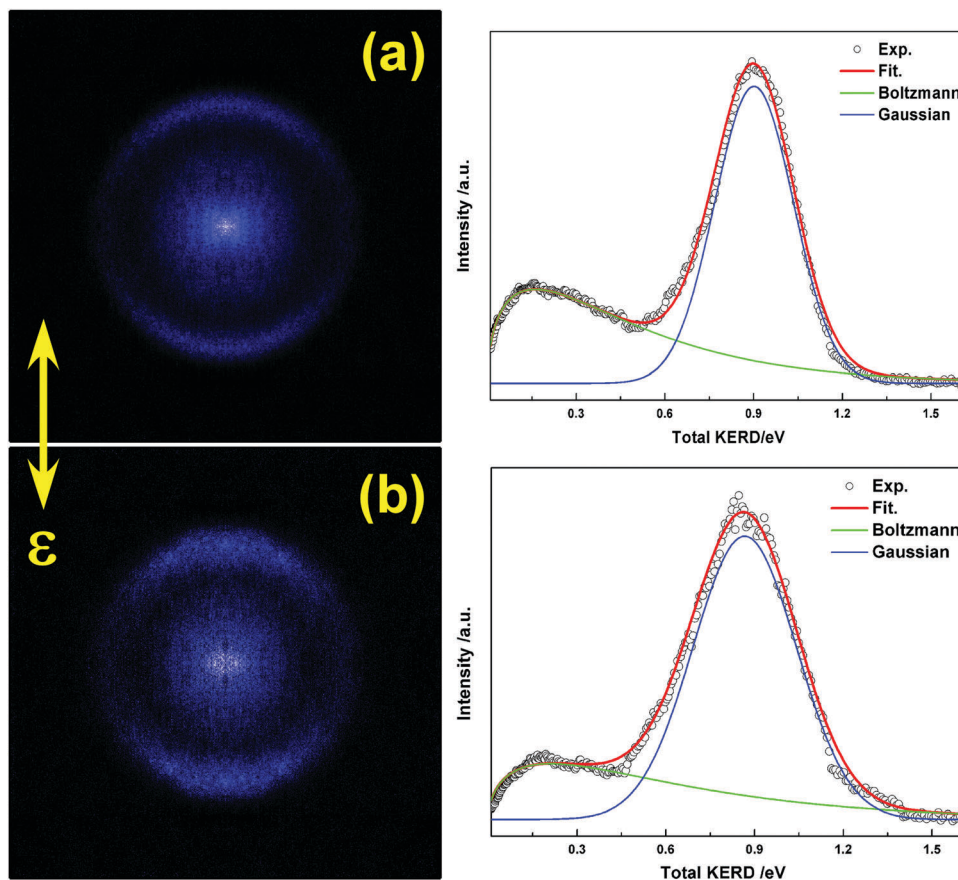
Fig. 6 3D TPEPICO time–sliced velocity map images of CF_3^+ and the corresponding total kinetic energy release distributions, (a) at 14.88 eV and (b) at 15.36 eV.

Table 2 Average total released kinetic energy $\langle E_T \rangle$ and anisotropy parameters β in the rapid dissociation pathway of CF_3Cl^+ cations in various electronic excited states

$h\nu$/eV	State	E_{avail}/eV	$\langle E_T \rangle$/eV	$f_T{}^a$	ρ^b	β
14.88	A^2A'/B^2A''	2.09	0.90	0.43	0.61	1.30 ± 0.05
15.36	A^2A'/B^2A''	2.57	0.87	0.34	0.72	1.43 ± 0.05
16.99	$C^2A'/^2A''$	4.20	0.56	0.13	0.80	0.34 ± 0.01
17.85	$D^2A'/^2A''$	5.06	0.60	0.12	0.82	0.15 ± 0.01

^{a} $f_T = \langle E_T \rangle / E_{avail}$. ^{b} ρ is the fraction of the Gaussian-type component in the total dissociation products.

frequency ($\nu_2^+ = 809$ cm^{-1}),[72] the most populated vibrational states of CF_3^+ are located at $\nu_2^+ = 12$ at 14.88 eV and $\nu_2^+ = 17$ at 15.36 eV.

From the images, the angular distribution of CF_3^+ is acquired by integrating the intensities over a specific speed range at each angle. Then the anisotropy parameter β along the corresponding pathway is obtained by fitting the angular distribution, $I(\theta)$, with the following formula (2),[76]

$$I(\theta) = \frac{1}{4\pi}[1 + \beta \cdot P_2(\cos\theta)] \quad (2)$$

where θ is the angle between the recoil velocity of the fragment and the electric vector ε of the photon, and $P_2(\cos\theta)$ is the

second-order Legendre polynomial. It is well known that the statistical dissociation has an isotropic angular distribution with $\beta = 0$, while the rapid dissociation has a large β value (e.g., $\beta = 2$ for parallel and $\beta = -1$ for perpendicular distributions of diatomic molecule decomposition). Thus, we only pay attention to that of the Gaussian-profile component in the images, and Table 2 lists the fitted β values. At 14.88 and 15.36 eV, the present β values are 1.30 and 1.43, implying that the fast dissociations at the two energies both have parallel distribution. This is consistent with the direct photoionization from the ground state (X^2A_1) of the neutral ground state to the A^2A_1 ionic state. The increasing β values also agree with the more dominant proportion of the repulsive A^2A_1 state at the higher excitation energy.

To our surprise, the average total released kinetic energy $\langle E_T \rangle$ and the maximal kinetic energy are almost unchanged when the photon energy is increased from 14.88 eV to 15.36 eV. This is very similar to the dissociative photoionization of CF_4 via its B^2E ionic state.[30] Compared to the value at 14.88 eV, the f_T fraction at 15.36 eV is slightly decreased as shown in Table 2, although both of them are near the predicted value of the "impulsive model". The invariable fraction indicates that the partial excess energy must be kept as internal energy of the fragments and not be released in dissociation. A probable explanation is that the released kinetic energy along the
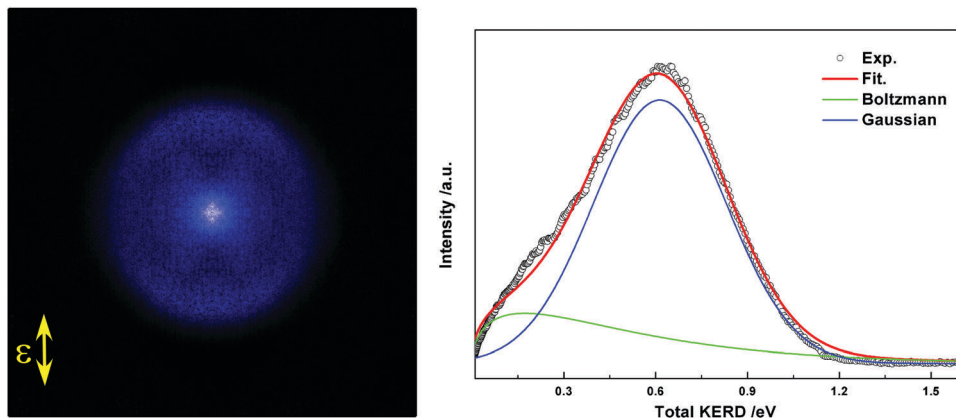
Fig. 7 3D time-sliced TPEPICO velocity map image of CF_3^+ and the corresponding total kinetic energy release distribution at 16.99 eV.

repulsive A^2A_1 state is determined by the energy of the effective curve-crossing from the B^2A_2 to A^2A_1 states, and thus if the crossing rate is much faster at certain energies along the dissociation coordinate, the rest of the internal energy will be accommodated in the internal energy of the fragment.

G. TPEPICO velocity map image of CF_3^+ dissociated from C^2E and D^2E states

Because the (3e) and (4e) outer molecular orbitals of CF_3Cl both consist of the lone-pair electron orbital of the F atom, the characteristics of the C^2E and D^2E states are similar. At a fixed photon energy of 16.99 eV, CF_3Cl^+ in the C^2E state is produced and subsequently dissociates to produce CF_3^+ and CF_2Cl^+ fragments. As mentioned above, only the lowest Cl-loss pathway, $CF_3^+(X^1A_1)$ + Cl, is discussed in this manuscript. The 3D time-sliced image of CF_3^+ is shown in Fig. 7, and a similar bimodal distribution is found for its total KERD. Compared to the images in Fig. 6, the Gaussian-type kinetic energy distribution becomes wider.

However, the maximum of the total KERD is *ca.* 1.1 eV at 16.99 eV and lower than that of the A^2A_1/B^2A_2 state. This is abnormal because the A^2A_1, B^2A_2 and C^2E states have the same dissociation limit, and the available energy at 16.99 eV is dramatically increased by 2.11 eV from the 14.88 eV energy of

A^2A_1/B^2A_2. Through fitting the angular distribution of the outer ring in the image, the anisotropy parameter β is only 0.34 for the rapid dissociation channel in the DPI of CF_3Cl at 16.99 eV, which is far lower than the value for A^2A_1/B^2A_2 and implies a much slower dissociation rate. Since the C^2E state is bound along C–Cl bond rupture, the internal conversion from C^2E to the repulsive A^2A_1 state must occur to cause the production of the CF_3^+ fragment. Taking into account the lower KERD and the small β value, more than half of the excess energy should be kept as the internal energy of fragments in dissociation. There are two candidates for the energy release mechanism. One is fluorescent emission from C^2E to A^2A_1/B^2A_2 followed by dissociation along A^2A_1. However, an anisotropy distribution was observed for the CF_2Cl^+ fragment in the experiment, implying that the lifetime of C^2E should be shorter than the molecular rotational period. As a result, the fluorescence decay should be impossible. Therefore, the unique possible mechanism is that both Cl-loss and F-loss fragmentation processes interact with each other, effectively decreasing the kinetic energy release along the Cl-loss pathway.

A similar image and a total KERD curve are observed for the DPI of CF_3Cl at 17.85 eV, shown in Fig. 8. The outer ring becomes more degraded, but its diameter is kept as that in Fig. 6 and 7. The total KERD curve looks almost the same as
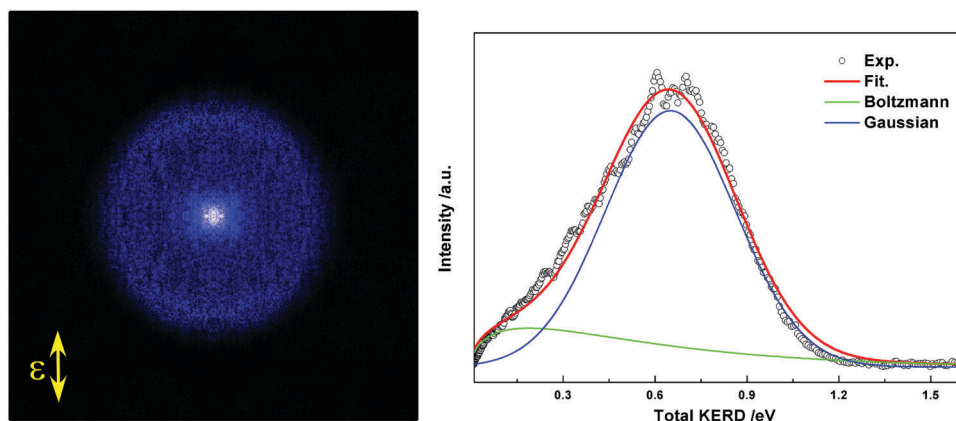

Fig. 8 3D time-sliced TPEPICO velocity map image of CF_3^+ and the corresponding total kinetic energy release distribution at 17.85 eV.

that at 16.99 eV, although the available energy is very much increased. Moreover, the anisotropy parameter β is determined to be 0.15 and close to zero for the outer ring, indicating that the rate of C–Cl bond rupture for $CF_3Cl^+(D^2E)$ is longer than that of a molecular rotational period. Thus, an energy release mechanism similar to that of $CF_3Cl^+(C^2E)$ is expected for the Cl-loss of $CF_3Cl^+(D^2E)$.

4. Conclusions

In this work, we have applied TPEPICO velocity map imaging to investigate the energy-selected dissociation dynamics of CF_3Cl^+ cations. The TPES in the energy range of 12.30–18.50 eV were recorded and covered the lowest electronic states like X^2E, A^2A_1, B^2A_2, C^2E and D^2E states. Subsequently, the TPEPICO TOF mass spectra were obtained at 13.26, 14.88 15.36, 16.99 and 17.85 eV, respectively. Two fragment ions, CF_3^+ and CF_2Cl^+, were observed respectively, and the latter only appeared in the energy range of the C^2E and D^2E states.

For the ground state, CF_3^+ fragments and CF_3Cl^+ ions coexisted. With an increase in excitation energy, the fraction of CF_3^+ rose while the parent ion vanished. Through fitting the breakdown curves in an energy range of 12.60–12.85 eV, $AE_0(CF_3^+/CF_3Cl)$ was determined to be 12.79 ± 0.02 eV. Thus, the assessment of the C–Cl bond dissociation energy of CF_3Cl^+ was 27.98 ± 3.86 kJ mol^{-1}. Taking into account the C–Cl bond energy of CF_3Cl in the database, 3.786 ± 0.039 eV, the adiabatic ionization energy (IE_0) of the CF_3 radical was calculated to be 9.06 ± 0.02 eV.

3D TPEPICO time-sliced velocity map images of CF_3^+ fragment ions dissociated from internal energy selected CF_3Cl^+ ions were recorded subsequently. Both the total KERD and the angular distribution were obtained. For the A^2A'/B^2A'' states, the images shows two components, and the total KERD fits very well with Boltzmann- and Gaussian-type curves. As suggested by the theoretical calculations, the B^2A'' state is bound while the A^2A' state is typically repulsive along the C–Cl bond rupture. Therefore, the Boltzmann-type distribution in the image corresponds to the statistical dissociation of the bound B^2A'' state via internal conversion to a high vibrationally excited ground state. The Gaussian one contributed by the direct dissociation along the repulsive A^2A' state takes a large proportion, and thus the non-statistical dissociation pathway dominates in this energy region. Moreover, the anisotropy parameters of the Gaussian-type component are 1.30 at 14.88 eV and 1.43 at 15.36 eV, and are consistent with the direct photoionization from the neutral CF_3Cl (X^2A_1) to the A^2A_1 ionic state. The increasing β values also agree with the larger proportion of the repulsive A^2A_1 state at the higher excitation energy.

For the C^2E and D^2E states, the images of CF_3^+ also include one statistical and one non-statistical dissociation component, and thus two dissociation mechanisms are suggested for the C–Cl bond rupture of CF_3Cl^+ in the C^2E and D^2E states. As the C^2E and D^2E states are bound along Cl-loss potential energy curves, the internal conversion from C^2E or D^2E to the repulsive A^2A_1 state must occur in order to produce the CF_3^+ fragment. Taking into account the lower KERD and the small β values, more than half of the excess energy is kept as the internal energy of fragments in dissociation for the DPI of CF_3Cl via the C^2E and D^2E ionic states.

Conflicts of interest

There are no conflicts to declare.

Acknowledgements

References

1 J. W. Coburn, *Plasma etching and reactive ion etching*, American Institute of Physics, New York, 1982.
2 A. C. Adams and C. D. Capio, *J. Electrochem. Soc.*, 1981, **128**, 366–370.
3 J. R. Roth, *Industrial Plasma Engineering*, Volume 1 Principles, Institute of Physics Publishing, Bristol, Philadelphia, 1995.
4 F. S. Rowland and M. J. Molina, *Rev. Geophys.*, 1975, **13**, 1–35.
5 T. Cvitaš, H. Güsten and L. Klasinc, *J. Chem. Phys.*, 1977, **67**, 2687–2691.
6 R. Jadrny, L. Karlsson, L. Mattsson and K. Siegbahn, *Phys. Scr.*, 1977, **16**, 235–241.
7 J. Doucet, P. Sauvageau and C. Sandorfy, *J. Chem. Phys.*, 1973, **58**, 3708–3716.
8 G. Cooper, W. Z. Zhang, C. E. Brion and K. H. Tan, *Chem. Phys.*, 1990, **145**, 117–129.
9 H. W. Jochims, W. Lohr and H. Baumgärtel, *Ber. Bunsenges. Phys. Chem.*, 1976, **80**, 130–138.
10 J. C. Creasey, D. M. Smith, R. P. Tuckett, K. R. Yoxall, K. Codling and P. A. Hatherly, *J. Phys. Chem.*, 1996, **100**, 4350–4360.
11 S. Cradock, E. A. V. Ebsworth and R. A. Whiteford, *J. Chem. Soc., Dalton Trans.*, 1973, 2401–2404.
12 Y. Uehara, N. Saito and T. Yonezawa, *Chem. Lett.*, 1973, 495–500.
13 W. Kischlat and H. Morgner, *J. Electron Spectrosc. Relat. Phenom.*, 1985, **35**, 273–288.
14 C. J. Noutary, *J. Res. Natl. Bur. Stand., Sect. A*, 1968, **72A**, 479–485.
15 J. M. Ajello, W. T. Huntress Jr and P. Rayermann, *J. Chem. Phys.*, 1976, **64**, 4746–4754.
16 F. C. Y. Wang and G. E. Leroi, *Ann. Isr. Phys. Soc.*, 1983, **6**, 210.
17 K. Watanabe, T. Nakayama and J. Mottl, *J. Quant. Spectrosc. Radiat. Transfer*, 1962, **2**, 369–382.
18 V. H. Dibeler, R. M. Reese and F. L. Mohler, *J. Res. Natl. Bur. Stand.*, 1956, **57**, 113–118.

19 W. Z. Zhang, G. Cooper, T. Ibuki and C. E. Brion, *Chem. Phys.*, 1991, **151**, 343–356.

20 I. Powis, *Mol. Phys.*, 1979, **39**, 311–327.

21 H. Schenk, H. Oertel and H. Baumgärtel, *Ber. Bunsenges. Phys. Chem.*, 1979, **83**, 683–691.

22 N. L. Ma, K.-C. Lau, S.-H. Chien and W.-K. Li, *Chem. Phys. Lett.*, 1999, **311**, 275–280.

23 Y.-L. He and L. M. Wang, *Struct. Chem.*, 2009, **20**, 461–479.

24 I. Novak, J. M. Benbon and A. W. Poits, *J. Electron Spectrosc. Relat. Phenom.*, 1986, **41**, 175–179.

25 G. M. Bancroft, J. D. Bozek, J. N. Cutler and K. H. Tan, *J. Electron Spectrosc. Relat. Phenom.*, 1988, **47**, 187–196.

26 J. D. Bozek, G. M. Bancro, J. N. Cutler, K. H. Tan, B. W. Yates and J. S. Tse, *Chem. Phys.*, 1989, **132**, 257–270.

27 I. Powis and C. J. Danby, *Chem. Phys. Lett.*, 1979, **65**, 390–394.

28 X. F. Tang, X. G. Zhou, M. M. Wu, S. L. Liu, F. Y. Liu, X. B. Shan and L. S. Sheng, *J. Chem. Phys.*, 2012, **136**, 034304.

29 X. F. Tang, X. G. Zhou, Z. F. Sun, S. L. Liu, F. Y. Liu, L. S. Sheng and B. Yan, *J. Chem. Phys.*, 2014, **140**, 044312.

30 X. F. Tang, X. G. Zhou, M. M. Wu, Z. Gao, S. L. Liu, F. Y. Liu, X. B. Shan and L. S. Sheng, *J. Chem. Phys.*, 2013, **138**, 094306.

31 G. A. Garcia, B. K. Cunha de Miranda, M. Tia, S. Daly and L. Nahon, *Rev. Sci. Instrum.*, 2013, **84**, 053112.

32 X. F. Tang, X. G. Zhou, M. L. Niu, S. L. Liu, J. D. Sun, X. B. Shan, F. Y. Liu and L. S. Sheng, *Rev. Sci. Instrum.*, 2009, **80**, 113101.

33 A. Bodi, P. Hemberger, T. Gerber and B. Sztáray, *Rev. Sci. Instrum.*, 2012, **83**, 083105.

34 H. F. Xu, Y. Guo, Q. F. Li, Y. Shi, S. L. Liu and X. X. Ma, *J. Chem. Phys.*, 2004, **121**, 3069–3073.

35 H. Wang, X. Zhou, S. Liu, B. Jiang, D. Dai and X. Yang, *J. Chem. Phys.*, 2010, **132**, 244309.

36 X. F. Tang, M. L. Niu, X. G. Zhou, S. L. Liu, F. Y. Liu, X. B. Shan and L. S. Sheng, *J. Chem. Phys.*, 2011, **134**, 054312.

37 X. F. Tang, X. G. Zhou, M. L. Niu, S. L. Liu and L. S. Sheng, *J. Phys. Chem. A*, 2011, **115**, 6339–6346.

38 X. F. Tang, X. G. Zhou, M. M. Wu, Y. Cai, S. L. Liu and L. S. Sheng, *J. Phys. Chem. A*, 2012, **116**, 9459–9465.

39 H. Offerhaus, C. Nicole, F. Lepine, C. Bordas, F. Rosca-Pruna and M. Vrakking, *Rev. Sci. Instrum.*, 2001, **72**, 3245–3248.

40 B. Sztáray and T. Baer, *Rev. Sci. Instrum.*, 2003, **74**, 3763–3768.

41 A. Bodi, B. Sztáray, T. Baer, M. Johnson and T. Gerber, *Rev. Sci. Instrum.*, 2007, **78**, 084102.

42 M. J. Frisch, G. W. Trucks, H. B. Schlegel, G. E. Scuseria, M. A. Robb, J. R. Cheeseman, G. Scalmani, V. Barone, B. Mennucci and G. A. Petersson, *Gaussian 09 D.01*, Gaussian, Inc., Wallingford, CT, 2009.

43 H. Koch and P. Jørgensen, *J. Chem. Phys.*, 1990, **93**, 3333–3344.

44 J. F. Stanton and R. J. Bartlett, *J. Chem. Phys.*, 1993, **98**, 7029–7039.

45 H. Koch, R. Kobayashi, A. Sanchez de Merás and P. Jørgensen, *J. Chem. Phys.*, 1994, **100**, 4393–4400.

46 M. Kállay and J. Gauss, *J. Chem. Phys.*, 2004, **121**, 9257–9269.

47 P. Hemberger, A. Bodi, T. Gerber, M. Würtemberger and U. Radius, *Chem. – Eur. J.*, 2013, **19**, 7090–7099.

48 X. K. Wu, M. M. Wu, X. F. Tang, X. G. Zhou, S. L. Liu, F. Y. Liu and L. S. Sheng, *J. Phys. Chem. A*, 2017, **121**, 4743–4753.

49 B. Sztáray, A. Bodi and T. Baer, *J. Mass Spectrom.*, 2010, **45**, 1233–1245.

50 A. Bodi, Á. Kvaran and B. Sztáray, *J. Phys. Chem. A*, 2011, **115**, 13443–13451.

51 J. Harvey, A. Bodi, R. P. Tuckett and B. Sztáray, *Phys. Chem. Chem. Phys.*, 2012, **14**, 3935–3948.

52 X. K. Wu, X. G. Zhou, P. Hemberger and A. Bodi, *J. Phys. Chem. A*, 2017, **121**, 2748–2759.

53 O. K. Rice and H. C. Ramsperger, *J. Am. Chem. Soc.*, 1927, **49**, 1617–1629.

54 O. K. Rice and H. C. Ramsperger, *J. Am. Chem. Soc.*, 1928, **50**, 617–620.

55 R. A. Marcus and O. K. Rice, *J. Phys. Chem.*, 1950, **55**, 894–908.

56 B. Ruscic, R. E. Pinzon, M. L. Morton, G. von Laszevski, S. J. Bittner, S. G. Nijsure, K. A. Amin, M. Minkoff and A. F. Wagner, *J. Phys. Chem. A*, 2004, **108**, 9979–9997.

57 B. Ruscic, R. E. Pinzon, G. Von Laszewski, D. Kodeboyina, A. Burcat, D. Leahy, D. Montoy and A. F. Wagner, *J. Phys.: Conf. Ser.*, 2005, **16**, 561–570.

58 B. Ruscic, *Int. J. Quantum Chem.*, 2014, **114**, 1097–1101.

59 B. Ruscic and D. H. Bross, available at ATcT.anl.gov, 2016.

60 B. Ruscic, *J. Phys. Chem. A*, 2015, **119**, 7810–7837.

61 S. J. Klippenstein, L. B. Harding and B. Ruscic, *J. Phys. Chem. A*, 2017, **121**, 6580–6602.

62 T. A. Walter, C. Lifshitz, W. A. Chupka and J. Berkowitz, *J. Chem. Phys.*, 1969, **51**, 3531–3536.

63 M. Horn, M. Oswald, R. Oswald and P. Botschwina, *Ber. Bunsenges. Phys. Chem.*, 1995, **99**, 323–331.

64 R. L. Asher and B. Ruscic, *J. Chem. Phys.*, 1997, **106**, 210–221.

65 B. Ruscic, J. V. Michael, P. C. Redfern, L. A. Curtiss and K. Raghavachari, *J. Phys. Chem. A*, 1998, **102**, 10889–10899.

66 A. Ricca, *J. Phys. Chem. A*, 1999, **103**, 1876–1879.

67 D. A. Dixon, D. Feller and G. Sandrone, *J. Phys. Chem. A*, 1999, **103**, 4744–4751.

68 P. Botschwina, M. Horn, R. Oswald and S. Schmatz, *J. Electron Spectrosc. Relat. Phenom.*, 2000, **108**, 109–122.

69 G. A. Garcia, P.-M. Guyon and I. Powis, *J. Phys. Chem. A*, 2001, **105**, 8296–8301.

70 E. E. Ferguson, T. M. Miller and A. A. Viggiano, *J. Chem. Phys.*, 2003, **118**, 2130–2134.

71 J. M. Bowman, X. C. Huang, L. B. Harding and S. Carter, *Mol. Phys.*, 2006, **104**, 33–45.

72 H. Dossmann, G. A. Garcia, L. Nahon, B.K. C. de Miranda and C. Alcaraz, *J. Chem. Phys.*, 2012, **136**, 204304.

73 J. Clay, E. Walters, J. Grover and M. Willcox, *J. Chem. Phys.*, 1994, **101**, 2069–2080.

74 G. K. Jarvis and R. P. Tuckett, *Chem. Phys. Lett.*, 1998, **295**, 145–151.

75 E. A. Walters, J. T. Clay and J. R. Grover, *J. Phys. Chem. A*, 2005, **109**, 1541–1547.

76 R. N. Zare, *Mol. Photochem.*, 1972, **4**, 1.